Analysis of Internal Fluid Motion in an Archimedes Screw using Computational Fluid Mechanics

Published as:

Simmons SC, Lubitz WD. Analysis of internal fluid motion in an Archimedes screw using computational fluid mechanics. Journal of Hydraulic Research. 2021 Nov 2;59(6):932-46.

SCOTT CHRISTOPHER SIMMONS, PhD. Candidate, *School of Engineering, University of Guelph, Guelph, Canada*

Email: ssimmons@uoguelph.ca (author for correspondence)

WILLIAM DAVID LUBITZ, Associate Professor, *School of Engineering, University of Guelph, Guelph, Canada*

Email: wlubitz@uoguelph.ca

Internal fluid motion in Archimedes screws

Analysis of Internal Fluid Motion in an Archimedes Screw using Computational Fluid Mechanics

ABSTRACT

Two computational fluid dynamics models were developed to analyse the internal fluid mechanics of an Archimedes screw's buckets. The models were evaluated against laboratory-scale experimental data, which suggested that they were acceptably accurate. Results of power-generating torque, internal fluid velocities, wall shear stress, and leakage flow rates were all explored with respect to changing rotational speeds. It was found that increasing rotational speed while maintaining "full" screw buckets would produce: similar torque values (by extension: power increased), higher velocity magnitudes of fluid parcels in a bucket, less gap leakage flow rate, and higher wall shear stress rates (by extension: more frictional losses).

Keywords: Archimedes screw; computational fluid dynamics; gap flow; screw generator; steady state

1 Introduction

Archimedes screw generators (ASGs) have been used in run-of-river hydropower schemes since the 1990's (Radlik, 1997). They are financially efficient, reliable and have low environmental impact [2]. Future Energy Yorkshire compared installation costs of a Kaplan turbine and an ASG at a specific UK site. The ASG had a 10% lower installation cost and supplied 15% more energy than the Kaplan turbine, making it 22% less expensive per unit power produced [3]. ASGs have relatively low maintenance requirements due to larger clearances and lower operating speeds than other microhydro turbines. Aside from regular inspections, a large maintenance commission should performed approximately every 20 years [4–7].

Unlike most common hydropower turbines, fish and sediment can pass directly through an operating ASG. Archimedes screws are commonly used to transfer fish between holding pens with a very low incidence rate of harm [8]. More recent studies have found ASGs are also fish-friendly [9,10]. A study of eel and kelt passage through the River Dart ASG (UK) found that both eels and fish were sometimes struck by the leading edge of the screw, which caused minimal injuries and a low mortality rate. It was suggested to add a rubber bumper to the leading edge of the screw flights to further minimize entrance trauma to marine life. Addition of the leading edge bumper resulted in less than 1% of eels sustaining injury (which was minimal and recoverable), and no injury to salmon kelts [10]. This study was used to inform guidelines on maximum rotation speeds for ASG installations [11].

ASGs are most appropriate at low head sites (about 5 m or less) with moderate flow rates (on the order of 10 $m^3 s^{-1}$ or less). There are few viable alternative turbine technologies in this range: practical options include very low head (VLH) turbines and Kaplan turbines [12], as well as overshot and undershot water wheels [13]. Denny (2004) found overshot and undershot water wheels have maximum achievable *mechanical* efficiencies of about 71% and 30%, respectively. Conversely, *water-to-wire* efficiency values of actual ASG plants is between 60% and 80% [14].

Screw generators are usually installed in an inclined orientation with the rotating screw contained in a fixed enclosing trough (Fig. 1). As the screw turns, water flows into the top of the screw from a forebay and fills the spaces between adjacent screw blades. The height of water in the screw forebay is termed the upper or inlet water level (h_U). The helical volume between two adjacent screw blades is termed a "bucket" [15]. The static water pressure distribution on the screw blade surfaces imparts a net torque on the screw blades, causing the screw to rotate, turn an attached generator, and generate electricity. The buckets translate axially downward along the length of the turning screw between the moving blades and the fixed trough, and the water eventually exits out the bottom of the screw into a receiving basin (Fig. 1).

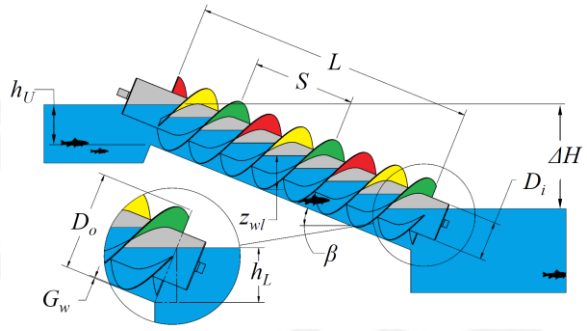

Figure 1 Common Archimedes screw variables

The optimal lower basin water level (h_L) results in submergence of the lower 55% to 60% of the screw outlet (i.e. $h_L / D_o \cos\beta = 0.55$ to 0.60) [16–18]. This produces a slight back-pressure at the ASG outlet that maintains the water level of each bucket until it exits the screw, but is not so high that receiving basin water will flow back in to the top of the screw outlet.

The water level within a bucket is quantified with the non-dimensional fill height *f*. Figure 2 shows the elevation variables z_{wl}, z_{max}, and z_{min} which are respectively the height of the actual water level, the maximum height of the water before it will begin to overflow the inner cylinder, and the minimum height of the bucket. The nondimensional fill height *f* is then defined as [19]

$$f = \frac{z_{wl} - z_{min}}{z_{max} - z_{min}} \qquad (1)$$

Songin (2017) presents improved equations to calculate z_{min} and z_{max} based on screw geometry that account for how the the helical geometry of the screw shifts the maximum fill point away

from top or bottom dead center. An empty bucket has $f = 0$, while a bucket filled with water just to the point where water would start to overflow over the central cylinder is considered full, with $f = 1$. Theoretically, f close to 1 is the most efficient operating condition [20], although some experimental studies observed maximum ASG efficiency with slight overfilling (i.e. when $f > 1$) [21].

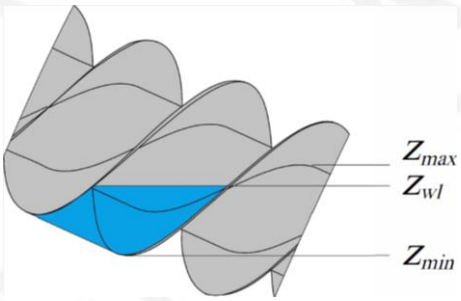

Figure 2 Bucket water level definitions

When $f > 1$ overflow leakage losses occur as water flows over the top of the inner cylinder from one bucket into a lower bucket. However, this efficiency loss is offset by the higher water levels in the buckets producing greater net torque than at lower fill levels.

In all fixed-trough Archimedes screws, a narrow gap exists between the outer edge of the screw blade tips and the fixed trough. This gap allows the screw to turn freely but permits some water to leak between buckets. The width of this gap (G_w) is minimized to lessen the gap leakage losses.

Screws are geometrically defined by outer diameter (D_o), the inner diameter (D_i) pitch (S), inclination angle (β), and number of blades (N) (Fig. 1). In a case study using Bayesian optimization techniques, it was found that the optimal ratio between inner diameter and outer diameter for the ASGs in the sample set was $D_i / D_o \approx 0.54$ [22]. Interestingly this is the same value theoretically determined by Rorres (2000) for the optimal design of an Archimedes screw pump. Note this theoretical optimum does not fully account for energy losses in operating screws, and in practice slightly lower ratios are often used, with $D_i / D_o \approx 0.50$ being perhaps the most common.

The complex, helical geometry of ASGs makes it difficult to experimentally observe the details of fluid motion within a bucket of an operating ASG, even at laboratory scale. Recently, a small free-floating neutrally buoyant sensing system called “Sensor Fish” was developed to directly measure the hydraulic conditions experienced by fish in different hydroelectric plants, and validation testing included an ASG installation [12]. The Sensor Fish was able to measure three components of both linear acceleration and angular velocity, plus absolute pressure and temperature at a frequency of 2048 Hz [12]. The sensor was designed to be neutrally buoyant, so it can follow the flow paths of fluid through the hydropower installations. The study provided unique insight into the pressure characteristics within the buckets of a real-world ASG.

Prior experimental studies of Archimedes screws have measured bulk parameters such as torque, rotation speed and water levels [21,23–26]. But it is not possible to directly measure important parameters such as gap leakage flow, wall shear stress, and overflow leakage flow [21]: this is currently a limiting factor in further model development. The authors are not aware of any information in the literature on the dynamics of water movement within an Archimedes screw bucket. This study seeks to begin to fill this knowledge gap by using computational fluid dynamics (CFD) to visualize and quantify the fluid motion within the buckets of an Archimedes screw. The CFD model is validated against laboratory-scale data used to develop prior parametric models [16].

2 Methods

CFD models of both a single bucket, and a four-bucket sequence, were developed for visualizing and quantifying the internal fluid mechanics in an ASG bucket. The single-bucket model simulates one bucket in an idealised screw without a gap region between the blades and the trough. The four-bucket model then introduces this gap region to see its effect on fluid flow within the screw. The four-bucket model is an extension of the single-bucket model both theoretically and geometrically. It is created by simulating four adjacent single-buckets together, with gap regions introduced between blade edges and the trough surface. Both models used the same mesh generation methods, and similar boundary conditions and simulation physics. These simulation similarities allow the single-bucket model validation to lend credibility to the four-bucket model.

Both models simulate internal flow in an ASG under equilibrium conditions, but note that true equilibrium is rarely achieved in real ASGs. The inrush of water through the screw inlet, mediated by the rotating leading edges of the blades, results in an episodic filling event as a bucket is formed that is very transient. The water now contained in the bucket has initial momentum and can be seen to slosh back and forth in the bucket. Equilibrium within the bucket would not be reached until the sloshing was fully damped and initial spatial variations in water velocity diffuse to a steady state condition. In real-world screws, water is not present in the screw long enough to reach this dampened equilibrium condition before the water exits the screw at the outlet. Though equilibrium is not reached in practice, it is valuable to understand flow conditions at equilibrium since this is the limiting condition for fluid motion within ASG buckets.

2.1 Laboratory Experiments

Both the single-bucket and four-bucket model were validated with experimental data from the University of Guelph's Archimedes Screw Laboratory. An Archimedes screw was tested

by placing it between upper and lower basins. Water was pumped at a selected flow rate through an Omega FTB-740 inline turbine flow meter (with uncertainty of 1% of full scale) into an upstream supply basin that drained to the upper basin through a weir. The flow meter was calibrated in-situ prior to the experiments, and correct operation was verified during experiments with manual flow measurements based on supply basin water depths. Water level relative to the weir crest provided an independent measure of the flow rate through the recirculating loop.

Water depths in each basin were measured with Keller Series 26 Y depth sensors (with uncertainties of 0.25% of full scale) located within stilling wells. Screw rotation speed was maintained using a variable frequency drive (VFD) gear motor fixed to the screw frame by a moment arm and load cell link. The screw rotation speed was set using the VFD and torque produced by the ASG was measured with the combination of the load cell force and moment arm. The torque measurements had an overall uncertainty of $\delta T \approx 0.22$ N m [27]. Rotation speed was measured using a magnetic tachometer sampled at a very high frequency. The resulting rotation speed measurement uncertainty was found to be negligible relative to the depth and torque measurements [28]. The mechanical power produced by the screw is the product of the rotation speed and torque measurements.

Each test involved first setting a system water flow rate and the screw rotation speed. The system was then allowed to reach system-wide quasi-equilibrium in which the upper and lower water levels remained constant (aside from surface fluctuations due to wave-action). Data acquisition was then started, with sensor readings recorded at a frequency of 1000 Hz for 60 seconds. More specific protocols were followed to gather nominal sensor readings within 1% of desired data (speed and flow) points. This general process was carried out for each test run within an experimental data set.

The test screw had the same geometry as the CFD models (Table 1). Experimental data was collected for six different rotation speeds (20, 30, 40, 50, 60, and 80 RPM), five different flow rates (6, 8, 10, 12, 14 L s^{-1}), and three different outlet fill heights ($h_L/D_o \sin(\beta)$ = 0%, 30%, and 60%).

Table 1 Experimental and CFD screw dimensions

Outer Diameter D_o	Inner Diameter D_i	Length L	Pitch S	Number of Blades N	Inclination Angle β
31.8 cm	16.8 cm	122 cm	31.8 cm	3	24.5°

The data was post-processed to determine the mechanical power output of the ASG, the power available in the flow, the bucket fill height, bucket flow rate, estimated leakage flows, the overall screw efficiency, and other parameters. Once a test was completed, the settings were changed to map the next required data point. This process was carried out until a comprehensive

dataset was acquired. The resulting dataset comprises nearly 200 unique points for this screw. Additional experimental information is reported by Songin and Lubitz (2018).

3 Computational Fluid Dynamics Modelling

Two three-dimensional, transient CFD models were developed and implemented in OpenFOAM 4.0 (The OpenFOAM Foundation Ltd., London, United Kingdom). A two phase (water, air) volume of fluid approach was utilized to reproduce water free surfaces [29], and Menter's shear stress transport model was used for turbulent closure [30]. Both models were developed with high mesh resolution to allow investigation of phenomenon with length and time scales that can be several orders of magnitude smaller than the overall screw length and time scales. Inclusion of the blade-trough gap region in the four-bucket model allowed simulation of leakage flows in Archimedes screw generators (i.e. gap leakage and overflow leakage). Comparisons may be made between the single-bucket and four-bucket models to understand the effects of introducing the gap region. The models specifically simulate fluid motion within either one or four adjacent screw buckets under "quasi-steady" equilibrium conditions. Moving-wall boundary conditions are used to simulate ASG rotation. Simulating one or four buckets instead of an entire screw allows higher cell density and refinement, providing a more detailed characterisation of gap flow and flow within a bucket than would be possible simulating an entire screw plus inlet and outlet regions.

Only a one-bucket simulation is needed to simulate bucket flow in an idealized, gapless screw. Four buckets were found to be the minimum number required to achieve a representative simulation of internal flows within a bucket and gap flow between adjacent buckets. Investigating gap flow between buckets requires simulation of adjacent buckets. A two-bucket simulation would allow gap leakage to be visualized, but the height of water in the buckets needs to be controlled at the inlet and outlet of the simulation domain. Simulating four adjacent buckets results in two internal buckets in which flow will be representative, with gap flow between the two buckets, as well as adjacent inflow and outflow buckets. The simulation domains of both one-bucket and four-bucket models are shown in Fig. 3 within a screw for reference. The four-bucket model's buckets are numbered from top (left) to bottom (right) as 1 through 4.

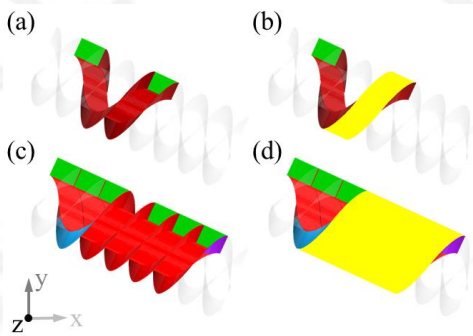

Figure 3 Screw (made transparent) with simulation domain superimposed for the single-bucket (a, b) and four-bucket (c, d) models. For clarity, the single-bucket model domain is shown with (b) and without (a) the trough boundary. The boundaries of this mesh are shown as: screw walls (red), atmosphere (green), and trough (yellow). The four-bucket model mesh is also shown with (d) and without (c) the trough boundary. Its boundaries are shown as: screw walls (red), atmosphere (green), trough (yellow), inlet (blue), and outlet (purple).

Bucket 1 of the four-bucket model domain is the "inlet reservoir" bucket. It has an inlet flow of water as defined by the inlet boundary condition; this condition was set to maintain a fill height of $f = 1$ within the bucket. The fill height is artificially maintained in this bucket, so that the successive buckets will experience the correct upstream conditions of a screw at its equilibrium state. However, as previously mentioned, since the height and flow of water in this bucket are maintained artificially, it should not be sampled and acts as a reservoir in the simulation. Bucket 4 is an "outlet reservoir" bucket with fill height maintained by defining an outlet surface as a weir. Water overtops the weir at the outlet and outflows into a zero-gauge pressure environment (i.e. essentially flowing into open-air). Water level in this bucket is therefore also artificially maintained at a level to allow the immediately upstream bucket 3 to experience the correct downstream conditions of an ASG at equilibrium.

The two middle buckets (bucket 2 and bucket 3) operate in conditions similar to those in the middle of an Archimedes screw operating at a steady rotation speed and flow, and should be representative of actual conditions within internal buckets in an operating screw. The following analysis will focus on the gap flow between bucket 2 and bucket 3, the overflow out of bucket 2, and the internal water motion in buckets 2 and 3.

Figure 4 shows the mesh for both the single-bucket and four-bucket models. A hexahedral block mesh with cell size varying smoothly between 2.6 mm by 1.5° by 3 mm (r, θ, z) in the interior and 0.4 mm by 1.5° by 0.53 mm in the gap region was generated to allow for 10 mesh points within the gap region. Cell size was smoothly transitioned between the fine gap region and the coarser interior region.

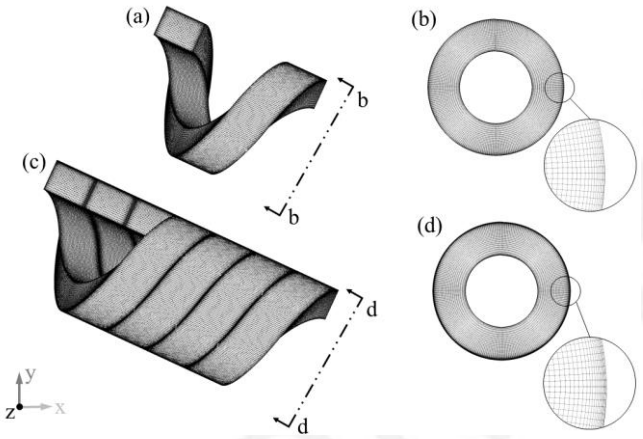

Figure 4 Single bucket mesh (a) shown with a section view (b) and detailed view of the near-wall refinement; note the single bucket mesh has no gap region. Four-bucket mesh (c) shown with a section view (d) and detailed view of the gap region and near-wall refinement.

The simulation boundaries consist of an inlet on bucket 1, an outlet on bucket 4, and the atmospheric components at the top of the channels, as well as the wall boundaries at the blades, inner cylinder of the screw, and the trough. The single-bucket model was meshed with the same refinement parameters so that the mesh is geometrically identical to any of the buckets of the four-bucket model. This allows for direct comparisons between the results of the CFD simulations and allows both models to be developed with the exact same solver and boundary conditions. The only exception is that the single bucket model has no inlet or outlet boundaries since there is negligible flow exiting the screw during the simulation. Seven simulations were carried out at an inclination angle of $\beta = 24.5°$ for both the single- and four-bucket models; one at each rotation speed of 0, 20, 30, 40, 50, 60, and 80 RPM.

3.1 Governing Equations and Solver

This problem was found to have Reynolds numbers of around $Re = 3000$ in the blade-trough gap region and $Re = 46000$ in the buckets. In the gap, the characteristic length and velocity were the gap width (G_w) and the average velocity through the gap ($\overline{v_g}$), respectively. In the buckets, the characteristic length and velocity were the hydraulic diameter of the screw ($D_o - D_i$) and the transport velocity (v_t). The Froude number of a bucket was about $Fr = 0.30$, meaning that the simulations were dealing with subcritical flows. The gap region was considered internal flow – so it was exhibiting low-Reynolds number turbulent flow.

OpenFOAM's *interFoam* solver was implemented to carry out the simulations; it is a two-phase solver of the Reynolds Averaged Navier-Stokes (RANS) equations that was implemented to numerically approximate a solution to this transient, two-phase problem. To address the transience of the model, an adaptive timestep was chosen. With typical values on the order of 10^{-4} s, the adaptive timestep ensured that the Courant-Friedrichs-Lewy (CFL) number never surpassed unity.

Conservation of mass was applied to the solver,

$$\frac{\partial \rho}{\partial t} + \nabla\cdot(\rho \boldsymbol{U}) = 0 \qquad (2)$$

where ρ is the fluid density, t is time, and **U** is the three-dimensional velocity field. In the case of this simulation, both water and air phases were considered incompressible, and so the conservation of momentum was applied for a two-phase incompressible Newtonian fluid.

$$\frac{\partial \rho \boldsymbol{U}}{\partial t} + \nabla\cdot(\rho \boldsymbol{U}\boldsymbol{U}) = -\nabla P + \nabla\cdot\tau + \rho \boldsymbol{g} + F \qquad (3)$$

In Eqn. 3, P is the pressure, τ is the sum of the viscosity stress tensor and Reynolds stress tensor, **g** is the gravitational acceleration vector, and F accounts for the surface tension force.

Finally, the traditional volume of fluid equation presented by Hirt and Nichols [29] was implemented to solve for the free surface. The method uses the continuum surface force model to evaluate the pressure gradient generated at the gas-liquid interface due to surface tension [31] (Eqn. 4).

$$\frac{\partial \alpha}{\partial t} + \nabla \cdot (\alpha \boldsymbol{U}) = 0 \qquad (4)$$

The variable α represents the phase of the fluid; $\alpha = 0$ represents the air phase, and $\alpha = 1$ represents water.

Both models used the PIMPLE algorithm; a combination of the PISO (Pressure Implicit with Splitting of Operator) and SIMPLE (Semi-Implicit Method for Pressure-Linked Equations) algorithms. The PIMPLE algorithm is a transient variant of the SIMPLE algorithm as it uses the SIMPLE algorithm to approximate a solution at each timestep.

The gradient terms in the system of equations were finite volume discretized and central differencing was applied for interpolation. The divergence schemes (advection and some diffuse terms) were finite volume discretised as well. Velocity gradients were calculated using the second order upwind scheme, and van Leer's [32] reported differencing scheme was used for advection of the phase fraction. The diffusion term in the momentum equation utilized central differencing for interpolation.

Menter's shear stress transport (k-ω SST) was used for turbulent closure [30] since it is one of the most commonly used and widely verified models in hydropower turbine modelling [33]. This model implements either the k-ω model or the k-ε model in the most appropriate flow regions to increase model accuracy. Briefly: the k-ω model is applied in the sublayer region, since it has been shown that k-ω is the more accurate turbulence model in this region. However, k-ω tends to lose accuracy as the solver reaches the outer layer, and so the shear stress transport model switches to the k-ε model using a blending algorithm, since the k-ε model has been shown to be more accurate in the free-stream flow region [30]. This provided a robustness desired by the authors when modelling both the buckets and the gap region since the Reynolds number varied significantly between the two regions signifying the flow characteristics may be vary between them.

The four-bucket simulation had an average $y^+ = 0.343$ along the trough and $y^+ = 1.49$ along the blades. It was carefully ensured that y^+ values in the gap never approached or exceeded $y^+ = 10$ since it was shown that SST performs very well when modelling incompressible boundary layer flow with values of $y^+ < 10$ and $y^+ > 100$ [34].

3.2 Boundary Conditions

The boundaries of the single- and four-bucket models are displayed in Fig. 3. Both the single- and four-bucket models have the same boundary treatments for the trough, inner

cylinder, blades and the atmosphere. The four-bucket model also includes inlet and outlet regions to maintain the fill heights in the bucket by accounting for the leakage losses that are introduced when adding the gap region. Table 2 summarizes simulation boundary conditions.

Table 2 Boundaries of single-bucket and four-bucket simulations with field values and field definitions. NOTE: the single-bucket model has neither inlet nor outlet regions.

Field	Symbol	Unit	Walls		Atmosphere	Inlet	Outlet
			Screw	Trough			
Dispersed phase volume fraction	**α**	**-**	zero-normal gradient	zero-normal gradient	conditional zero-normal gradient	uniform value of 1	conditional zero-normal gradient
Turbulence kinetic energy (TKE)	**k**	**$m^2 s^{-2}$**	Neumann boundary k-wall function	Neumann boundary k-wall function	conditional zero-normal gradient	uniform intensity of 0.05	conditional zero-normal gradient
Specific dissipation rate	**ω**	**s^{-1}**	Menter's shear stress transport	Menter's shear stress transport	conditional zero-normal gradient	uniform value of 0.003 s^{-1}	conditional zero-normal gradient
Dynamic pressure	**p_{rgh}**	**kg $m^{-1} s^{-2}$**	found by solver using velocity	found by solver using velocity	total pressure of 0 Pa	flux pressure of 0 Pa	total pressure of 0 Pa
Velocity	**U**	**m s^{-1}**	rotating wall velocity	moving wall velocity	conditional zero-normal gradient	inflow rate of 0.853 L s^{-1}	conditional zero-normal gradient

The dispersed phase volume fraction (α) is the variable used by *interFoam*'s volume of fluid method to define the two phases of the simulation. For the wall surfaces, the phase at the boundary was taken to be the value of the cell centre nearest to the boundary node (i.e. a zero-normal gradient condition). Since the mesh is well-refined, this is a reasonable assumption as the nearest cell centre is very close to the boundary. For the outlet and atmospheric boundaries, a hybrid condition was applied. The condition allowed both the water and air phases to exit, but only allowed air to re-enter through the boundary. Finally, the inlet boundary had a fixed, uniform value of $\alpha = 1$, meaning that all the flow into the system at the inlet was in the water phase.

A k-wall function that applied the Neumann boundary condition was implemented at the walls – a pure zero-gradient boundary condition [35]. Again, the boundaries for the atmosphere and outlet were set to apply a zero-normal gradient in cases of outflow, and the nearest internal cell value in cases of inflow. This is because the atmosphere boundary is a non-confined surface and acts similarly to the internal fields of the simulation with respect to turbulence kinetic energy. Finally, a turbulence intensity of 5% was selected for the inlet boundary to match similar CFD studies [36].

The eddy kinematic viscosity (ν_T) field at all boundaries was calculated by the solver because a solution existed based on the other boundary condition definitions.

The specific dissipation rate (ω) at wall boundaries was defined with Menter's shear stress transport system, which switches between viscous and logarithmic relationships according to the position of the dimensionless wall distance (i.e. y^+). The values of y^+ are very small through the 2 mm wide gap region because a high cell resolution (at least 10 nodes) is needed to simulate

the flow in this region. Menter's SST turbulence closure model because it can handle the varying values of y^+ more favourably than other models. At the outlet and atmosphere, ω was defined to be zero-gradient in cases of outflow, and the values of the adjacent internal cells – which were set to 0.003 s^{-1} based on the turbulence intensity and length-scale of the simulation – were used in cases of inflow.

The dynamic pressure (ρ_{rgh}) at the outlet and atmosphere boundaries were set to zero-gauge pressure to simulate a non-confined, open-air environment. The inlet was given a zero normal gradient as specified by the inlet velocity boundary condition [37].

Wall boundaries were given non-zero velocities to simulate the rotating screw. The blades and inner cylinder of the screw rotate about the centre axis with a constant rotation speed. A radially varying velocity condition was applied to the blade surfaces to reflect this situation. The trough boundary translated parallel to that same centre-axis with the corresponding transport velocity (v_T), found using:

$$v_T = \frac{S\omega}{2\pi} \qquad (5)$$

In the four-bucket model, the outlet and atmospheric boundaries were given a zero-normal gradient condition applied for outflow, while the component of the internal cell value that is normal to the boundaries was taken in instances of inflow. The inlet was set to a constant water inflow of 0.853 L s^{-1}, which was equal the total leakage flow (Q_L) of the system, since the only water leaving the system passed as overflow and gap flow. Experimentation suggested that this leakage flow rate would result in a slightly overfull inlet-reservoir bucket, where some fluid would exit as overflow leakage, but the gap leakage flow rate would support a full bucket in the remaining buckets of the simulation.

The single-bucket model runs were all initialized with the same water volume, corresponding to a fill height of f = 1 and neither inflow nor outflow. The four-bucket model runs were initialized with the same corresponding water volume per bucket as the single-bucket simulations. However, due to the non-zero inflow and resulting outflow (that accounts for leakage losses) they were run until an equilibrium was reached that allowed for more consistent bucket fill patterns.

3.3 Mesh Sensitivity

The CFD models were run for 30 seconds of simulation time with multiple levels of refinement to check for mesh convergence. All simulations reached equilibrium after about 10 to 15 seconds of simulated flow. Time averages of the last 10 seconds of simulations were used for analysis to ensure that only representative equilibrium conditions were sampled.

The distribution of static water pressure in each bucket generates a net torque on each of the screw blades. This torque value was determined for both sides of the blade between buckets

2 and 3 in the simulation and multiplied by the average number of buckets in the screw being simulated to find the overall torque production in the screw. The values of this overall torque were used as the comparison variable for the mesh sensitivity study shown in Fig. 5.

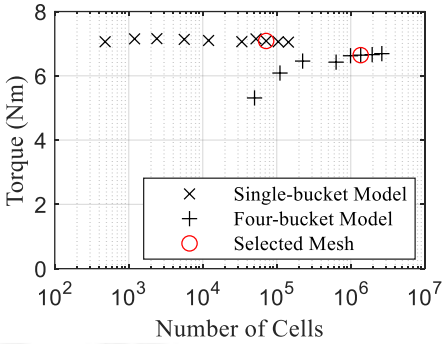

Figure 5 Mesh Sensitivity analysis using torque output for 80RPM single-bucket and four-bucket simulations

The data in Fig. 5 suggest that the four-bucket model mesh had converged at a one million cell refinement level. However, the mesh with 1.3 x 10^6 cells was used to simulate the flow in the bucket domain throughout the study, since it offered better resolution for flow visualization with little added computational time. The single-bucket mesh was selected to match the four-bucket mesh to allow for direct comparisons between the results. The selected single- and four-bucket meshes were shown in Fig. 4.

As Fig. 4 highlighted, a gradient was applied near the blade tips to refine the mesh in the gap region of the four-bucket model. The same gradient was applied to the single-bucket model for consistency.

3.4 Model Evaluation

Validation testing was similar for both the single-bucket and four-bucket models. The solver was run for 30 seconds of simulated flow in both models, and the last 10 seconds of simulated time was run with extra post processing scripts to sample all needed data fields. Unless otherwise noted in the following discussion, simulation results are the time-averaged values of parameters between 20 and 30 seconds in the simulations. For validation purposes, the torque and power generated by the screws were time-averaged and compared to the data.

While all the simulations were designed to run at a fill height of $f = 1$, the experimental data were obtained across a wide range of flow rates, rotation speeds and outlet conditions, and in any particular test, the fill height (which is dependent on each of these inputs) may not necessarily have been exactly $f = 1$. Therefore, the experimental results were linearly interpolated to obtain a best estimate of the power generated that would have been observed at a fill height of $f = 1$ corresponding to the simulations based on the set of data with fill closest to $f = 1$.

Fig. 5 shows a comparison between the experimental and simulated results. Note that in the laboratory, it was not possible to achieve low enough flow rates to test cases with $f = 1$ below 40 RPM, so the mechanical power is not presented for those speeds. The results from the single-bucket simulations were extrapolated to the entire screw assuming identical conditions in all buckets for comparisons to the experimental data. The experimental screw had an average of 11.52 buckets during its operation ($n_b = L / SN$) so the power predicted from a single bucket was multiplied by 11.52 to produce the power numbers shown in Fig. 6.

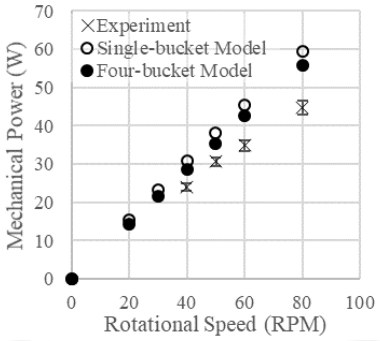

Figure 6 Experimental and simulated power changing with respect to rotation speed

Both the single-bucket and four-bucket simulations agree well with the experimental results (Fig. 6). The simulations predict a slightly higher power output than observed experimentally, and this difference increases with rotation speed. The single-bucket model over-predicts power up to 33% when compared to the experimental data, with an average deviation of 29%. The four-bucket model over-predicted power up to 25% when compared to the experiments with an average deviation of about 20%. It was expected that the simulations would predict higher power outputs than the experimental measurements, because the experimental data include several losses not included in the simulations that would reduce the measured shaft power, including losses at the screw inlet and outlet, and mechanical losses due to bearing friction.

Also, the simulations were run at equilibrium conditions. In the experimental screw (and in full-size screws), equilibrium is not likely reached since any given bucket of water forms, traverses the screw, and exits within a few seconds. It is suggested that the kinetic energy within a bucket may be much larger when it is not under steady conditions. This will result in some additional losses associated with it that are not included in a simulation of the case where equilibrium is reached.

The simulations are geometrically perfect cases, while the experimental screw has some imperfections along its blade surfaces that may change frictional losses. It also has a gap between the blades and the trough with an average width of 2 mm, incurring additional gap leakage losses not accounted for in the single-bucket simulation. The four-bucket simulations

include gap leakage loss but do not account for the minor imperfections in the experimental screw which may lead to varying gap widths along the perimeter of the blades.

Divergence between the model and experimental results in Fig. 6 increases as the rotation speed increases. This is expected since most of the losses discussed above (e.g. bearing and losses due to flow in and out of the screw) will increase with the rotation speed. However, the results are consistent with the unavoidable aspects of the differences between the experiments and simulations, suggesting that overall the model predicts power output and by extension the fluid motion in an Archimedes screw bucket well.

4 Results

The results of both the single- and four-bucket models will be presented and discussed alongside one another throughout this section. Additional results are presented in Simmons (2018) [27].

4.1 Torque with Respect to Rotation Speed

It is commonly suggested that screw torque is dominantly caused by the static pressure distribution in the bucket - so the ASG under normal operating conditions is considered a quasi-static system (Nuernbergk 2012) and observed net torque from a bucket would be the same at any rotation speed. However, some small dynamic effects might be expected to occur in the screw as the rotation speed changes.

Figure 7 shows bucket torque per wetted blade surface area versus rotation speed for the two CFD models. The torque was scaled by the wetted surface area of the screw blades to account for small variations in fill height. This was done because water exited the atmospheric boundaries as overflow leakage in both models, and this occurred more at high rotation speeds. As the rotation speed increases in Fig. 7, the wall shear stress increases and thus the friction losses on the blades would be expected to increase. While the total torque is not greatly affected by the rotation speed, there is an apparent trend of decreasing torque with increasing rotation speed in both simulations.

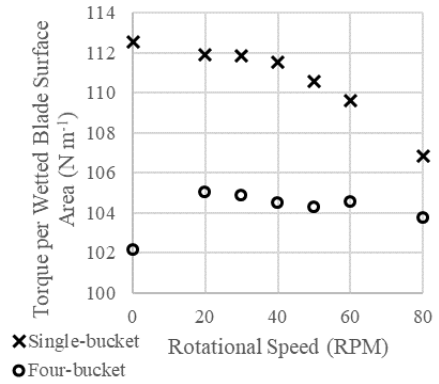

Figure 7 Effect of rotation speed on screw torque - scaled to wetted blade surface area in order to account for variations in fill height

The data in Fig. 7 suggest that torque is closely correlated to bucket fill level and that static pressure is the dominant driver for torque in ASGs. Since the data is all time-averaged for 10 seconds, the torque variations shown in Fig. 7, most notably for the single-bucket simulations, are suggested to be due to dynamic variations caused by the changing rotation speed. So, though the system is largely quasi-static, there is evidence that dynamic effects may exist on a small scale.

4.2 Bucket Internal Fluid Motion

Fluid motion within the buckets was analysed next to explore the dynamic effects mentioned above. Generally, fluid velocity magnitudes at any particular location in the bucket increased as the rotation speed of the screw increased. This might be expected, as relative motion between surfaces and the fluid volume increases with increasing rotation speed. Since screws are primarily driven by static pressure (i.e. converting mainly static pressure into mechanical power) any surplus fluid motion in the bucket could be considered an energy loss, because kinetic energy added to the fluid within the screw will not be recovered before the fluid exits the screw.

In both simulations, the kinetic energy of the mean flow within a bucket was very small (less than 0.3 W for a screw that produces less than 60 W). However, it is theorized that under equilibrium conditions, the kinetic energy would be smaller than under normal non-equilibrium operating conditions. This is because the relative velocities of the fluid in the bucket will decrease as the blade walls continue to transfer some of their kinetic energy to the fluid as steady state is reached.

It is very difficult to observe the flow structure in the interior of a bucket in a lab- or full-scale screw. Figure 8 shows the overall bucket flow patterns from both simulations for the case with the median 40 RPM rotation speed. Recall that the single-bucket simulations have no gap or gap flow, while these are present in the four-bucket results.

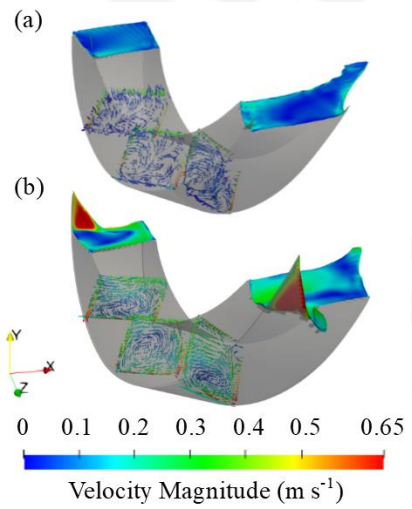

Figure 8 Velocity magnitude (colour) and direction (glyph arrows) of fluid within a single screw bucket for the 40 RPM case of the (a) single-bucket (no gap), and (b) four-bucket (gap present) simulations

In the single-bucket (i.e. the "no gap" screw bucket), water circulates in two primary cells across the bucket's cross-section – not necessarily aiding in the rotation of the blades. The rotating blade surfaces and inner cylinder cause the water to move rotationally along with the screw adjacent to these surfaces. The relative translation of the trough forces the water into a pinch-point where the trough meets the upstream blade edge, inducing a flow that pushes up onto the upstream blade, and then along the blade wall rotationally – this can be seen in more detail in Fig. 9.

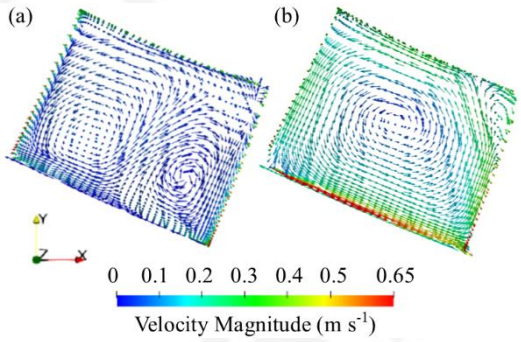

Figure 9 Magnified view of the middle sample plane of Fig. 8 for the (a) single-bucket (no gap) and (b) four-bucket (gap present) results.

The presence of a gap (i.e. the four-bucket simulation) changes the flow patterns in the bucket. The flow near the downstream gap is drawn out of the bucket and therefore adjacent fluid from the bucket volume is drawn towards the gap. The fluid is still entrained along the walls of the blades, but now there is now a greater downward velocity component toward the gap region. Moreover, there is a small layer of fluid moving at distinctly different velocity (on the order of 1 m s^{-1}) than the main volume of fluid (on the order of 0.1 m s^{-1}), that forms along the trough and moves through the gaps from upstream to downstream.

The total mean velocity kinetic energy in a bucket was about 2.16 mJ and 10.9 mJ (for the 40 RPM cases of the single- and four-bucket simulations, respectively). The kinetic energy in

the fluid increased several times with the introduction of the gap-region in the four-bucket simulation. This increase is mostly due to the introduction of the comparatively high velocity flow through the gap region.

The rotating and translating surfaces of the screw and trough do add a certain amount of non-turbulence associated mean velocity kinetic energy to the water in a bucket as it passes through the screw, and this energy is a loss in the sense that it is not available to produce torque on the blades and increase shaft power. However, the magnitude of the loss associated with this effect is very small: on the order of 1% assuming all buckets reached equilibrium before they reached the end of the screw. However, a real-world installation will see water rush into the top bucket with significant kinetic energy which is present throughout the translation of the bucket in the form of "sloshing". The water exits the bottom bucket with nearly the same kinetic energy as equilibrium is likely not reached – leading to no net losses. So, in practice, the power loss due to increasing bulk velocity in the bucket through shear interactions with the moving blades and trough is less than 1%.

4.3 Wall Shear Stress

Figure 10 shows the simulated wall shear stress on the blades for the 80 RPM case of both the single- and four-bucket simulations. The downstream portion of the blade (i.e. the portion that is on the lower side of the bucket and is driven by the pressure to produce positive torque) on the left, and the upstream blade surface (i.e. the part that will counteract the power-producing torque of the water) on the right.

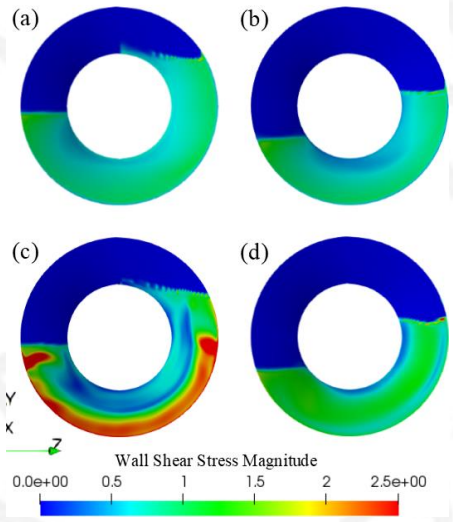

Figure 10 Time-averaged wall shear stress for the 40 RPM case of the single-bucket (a, b) and four-bucket (c, d) simulations. The left figures (a, c) show the blade face on the bottom end of the bucket and the right figures (b, d) show the blade face on the top end of the bucket.

Near the blade tips the wall shear stress of the four-bucket simulation reaches on the order of 5 Pa, which is higher than the 3 Pa wall shear stresses seen in the single-bucket simulation.

This demonstrates that the presence of the gap increases the shear stress on the blades on the tips of the downstream blade surface.

Figure 11 shows the power loss due to the friction on the blades caused by shear for varying rotation speeds, and the effect of those shear stress losses on overall power output. In both simulations, the power losses due to wall shear stresses increased as a function of a third order polynomial of the rotation speed. Dellinger et al. (2016) showed similar results using CFD, finding that the wall shear stress increased rapidly with the rotation speed [26].

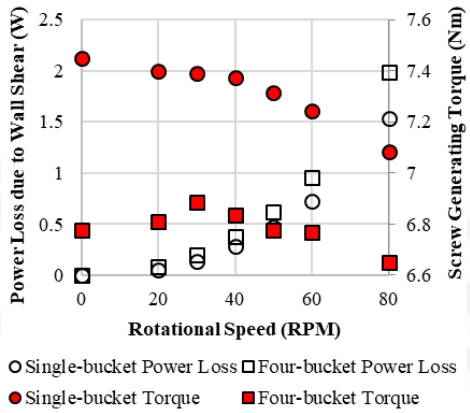

Figure 11 Torque and power loss associated with wall shear stress for the 40 RPM single- and four-bucket simulations

The single- and four-bucket cases in Fig. 11 have similar trends, but magnitudes differ slightly. The torque and power loss due to shear stress are lower in the four-bucket simulations than in the single-bucket simulations. It seems that, though the maximum shear stress is higher in the four-bucket simulations (Fig. 10), the overall shear stress is slightly lower than in the single-bucket simulation. This may be in part due to the change in flow patterns in the bucket caused by the introduction of the gap.

4.4 Leakage Flows

Flow through the gap is commonly modelled as being driven by the static pressure difference between adjacent buckets but does not account for screw rotation speed [19]. Figure 12 shows the velocity through the gap non-dimensionalised by the transport velocity corresponding to the screw rotation speed in each simulation.

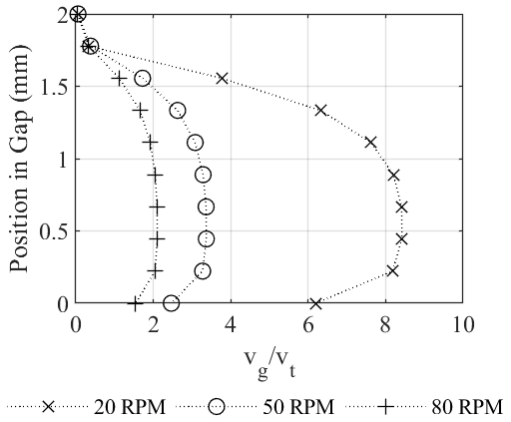

Figure 12 Velocity through the blade-trough gap relative to the transport velocity (the axial translation velocity of the blade tips). The position in the gap is measured from the bottom of the trough (0 mm) to the blade tip (2 mm).

The gap relative velocity is proportionally largest when the rotation speed is lower. Theoretically, there is a rotation speed at which there would be no net gap flow, since the blades are moving at a transport velocity that is faster than the fluid can move through the gap due to static pressure difference. So as the rotation speed increases, relative gap velocity and flow will decrease. It is suggested that this is the reason that the total kinetic energy in the buckets is decreasing as the rotation speed increases.

The maximum velocity in the gap reached about 0.9 m/s in the 50 RPM simulation. At the top of the gap (i.e. adjacent to the blade tips) velocity was zero relative to the blade tips. Fluid velocity increases in the middle of the gap, with a maximum nearly mid-way through the gap and then decreasing to match the transport velocity adjacent to the trough. The average velocity is higher than the transport velocity, and so the fluid adjacent to the trough is moving faster than the relative velocity of the blade tips. As the transport velocity is increased by increasing rotation speed, the velocity magnitudes in the gap decrease (Fig. 12).

The leakage flow Q_L is the sum of the gap leakage Q_{gl} and overflow leakage Q_o. The total flow through the screw Q is

$$Q = Q_b + Q_L = Q_b + Q_{gl} + Q_o \qquad (6)$$

where bucket flow rate Q_B is rate at which the volume in a bucket passes through the screw. In the four bucket simulations, Q_L is equal to the inlet flow to the system, since the only flow paths between the buckets are through the gap or as overflow over the central cylinder. The overall leakage flow was therefore set as the input flow to the system, and the overflow leakage was sampled out. Overflow leakage for each rotation speed is shown in Table 3; fill height is also included to verify the simulations were run under similar conditions.

Table 3 Bucket flow rate, gap and overflow leakage and fill height values for each rotation speed of the four-bucket simulations

Rotational Speed	Bucket Flow Rate (L s^{-1})	Gap Leakage (L s^{-1})	Overflow Leakage (L s^{-1})	Fill Height (-)
0	0	0.873	0.0007	1.04
20	3.09	0.648	0.0197	1.03
30	4.69	0.673	0.0161	1.03
40	6.21	0.649	0.0187	1.03
50	7.72	0.626	0.0142	1.03
60	9.21	0.585	0.0144	1.03
80	12.0	0.560	0.0151	1.01

For cases with inflow of Q_L = 0.853 L s^{-1}, and varying rotation speed, the overflow leakage increased as the rotation speed increased. Sloshing and overflow leakage were observed to increase both experimentally and in simulation with rotation speed. It is believed this is largely due to skin friction, an observation supported by previous studies [21]. The gap leakage in each simulation was calculated using the observed overflow leakage and recasting Eqn. 6. The gap leakage decreased as overflow increased since it is a function of the overall leakage and the overflow leakage. This agrees with the theory stated above – the gap flow will reach zero when the rotation speed is fast enough that the blades "outrun" the leakage flow rate. It is suggested that there would be a rotation speed corresponding to negative gap leakage. This is a state in which the velocity resulting from static pressure difference between adjacent buckets would be less than the transport velocity of the screw (v_t). In this case, fluid would leak into the previous bucket, rather than the next bucket. However, though the leakage may reach a zero or negative relative velocity, the fluid in the gap region does not interact with a blade surface in which the screw converts its pressure into a mechanical torque. Therefore, it may always be considered a form of power loss.

Next, the simulated gap leakage results were compared to the predictions of gap leakage model from Lubitz et al. (2014), which estimates gap leakage as

$$Q_{gl} = CG_w\left(l_w + \frac{l_e}{1.5}\right)\sqrt{\frac{2gS}{N}\sin\beta} \qquad (7)$$

This equation requires the wetted length (l_w) and the extended wetted length of the upper bucket (l_e), which are determined numerically, and a gap width G_w. The leakage constant C was set to 0.89 according to Kozyn [28], and the model was run under the same conditions as the simulation. Figure 13 shows the results of the simulation compared to the Lubitz model calculations for both bucket flow rate and gap leakage.

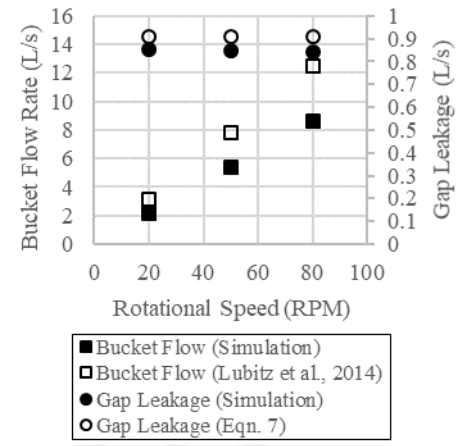

Figure 13 Bucket flow rate and gap leakage flow for each simulated speed

The Lubitz et al. (2014) model slightly overpredicted both the bucket flow and the gap leakage from the simulation, but it captured the correct trends from the simulations. Kozyn (2016) suspected that the model overestimates the gap leakage flow rate slightly, and these results support that conclusion. In Fig. 13, the gap flow is overpredicted by the CFD simulations by an average of about 8%, which is still a relatively accurate model prediction. However, since the simulation validations have uncertainties on this order, this conclusion should be regarded with caution as well.

5 Conclusions

This study used CFD simulations of the bucket regions in an Archimedes screw to provide insight into the internal fluid mechanics of Archimedes screw generators. The single-bucket simulation helped to visualize internal bucket flow without the effects of gap leakage. It was found that some variation between rotation speed and torque was present, suggesting that dynamic effects have a small impact on power loss, but it also showed that power output was primarily a function of the static pressure distribution in the bucket.

Simulating gaps between adjacent buckets had a notable effect on the internal flow within the screw. It changed the bulk flow in the overall bucket volume from a single to double cell configuration and introduced a completely different flow regime in the corners of the bucket. The change in flow near the bucket corners was mostly due to the pressure gradients near and across the gaps, as they were much greater than anywhere else in the bucket and drove changes to flow patterns.

The introduction of the gap region also changed some of the phenomenon associated with power loss within screw buckets: namely the kinetic energy and wall shear stress. When gap flow was present, it was associated with a significant portion of the total kinetic energy within a bucket. This may not necessarily demonstrate that the screw is adding kinetic energy to the water and a loss to its power production, but it is interesting to note the change. In a real-world screw, the water within the bucket would not achieve equilibrium conditions. Rather, it would

initially have a very large amount of kinetic energy as it entered the screw and formed a bucket. Water "sloshes" within the bucket until it is discharged at the bottom of the screw. So, it is suggested that the additional kinetic energy that is observed within the buckets of these equilibrium simulations would be negligible when compared to that of a real-world installation.

The introduction of the gap changed the maximum wall shear stress on the blades of each bucket. The overall shear stress on the blades decreased since the introduction of the gap changed the circulation pattern of the fluid in the bucket. However, it introduced high-stress regions where the water leaked from a higher bucket to its adjacent lower counterpart (i.e. the high pressure "red regions" of Figure 10) and along the blade tips. This showed that the frictional losses in the screw were changed due to the dynamic effects of the gap flow region.

Though the simulations have been shown to agree reasonably well with experimental results (cf. Fig. 6), they should still be taken as suggestions of the internal fluid tendencies of Archimedes screw generators since they are resolved by mathematical approximation. There are some drawbacks with all CFD modelling techniques. For this study Menter's Shear Stress Transport (SST), a two-equation RANS model, was used for turbulent closure. As with other eddy-viscosity models, recirculation and turbulence anisotropy can lead to excessive levels of turbulence production during the simulations [38]. As well, in two-phase flow problems the free surface dampens turbulence generation in the bucket. The SST model does not fully account for this phenomenon and may generate higher levels of turbulence as such [39].

However, with everything considered, these simulations provided valuable insight into the fluid mechanics within an Archimedes screw generator bucket and may be a valuable step forward into continued improvement and development of ASG performance models.

Acknowledgements

The authors gratefully acknowledge Tony Bouk and Brian Weber of Greenbug Energy Inc. and University of Guelph research associates Murray Lyons and Kathleen Songin for their contributions to this research.

Funding

This work was completed as part of a project financially supported by the Natural Sciences and Engineering Research Council (NSERC) Collaborative Research and Development (CRD) program [grant CRDPJ 513923-17] and Greenbug Energy Inc. (Delhi, ON, Canada).

Notation

C = leakage constant (-)

D_i = inner diameter (m)

654 D_o = outer diameter (m)
655 E_k = kinetic energy (J)
656 f = fill height ratio (-)
657 h_L = lower water level (m)
658 h_U = upper water level (m)
659 k = turbulence kinetic energy (J)
660 l_e = extended wetted length (m)
661 l_w = wetted length (m)
662 m = mass of water (kg)
663 n_b = number of buckets (-)
664 N = number of blades (-)
665 P = pressure (N m^{-2})
666 P_L = power loss (W)
667 P_{rgh} = dynamic kinematic pressure (m^2 s^{-2})
668 Q = total flow rate (m^3 s^{-1})
669 Q_B = bucket flow rate (m^3 s^{-1})
670 Q_{gl} = gap leakage flow rate (m^3 s^{-1})
671 Q_L = leakage flow rate (m^3 s^{-1})
672 Q_o = overflow leakage rate (m^3 s^{-1})
673 S = screw pitch (m)
674 t = time (s)
675 T = torque (N m)
676 u, U = fluid velocity (m s^{-1})
677 v_g = gap velocity (m s^{-1})
678 v_T = transport velocity (m s^{-1})
679 x = distance (m)
680 y^+ = dimensionless wall distance (-)
681 z_{min} = minimum bucket water level (m)
682 z_{max} = maximum bucket water level (m)
683 z_{wl} = bucket water level (m)
684 α = dispersed phase volume fraction (-)
685 β = inclination angle (°)
686 β^* = k-ω SST closure coefficient
687 γ = k-ω SST closure coefficient
688 λ_{ij} = turbulent stress tensor (N m^{-2})
689 μ_t = eddy viscosity (Pa s)

ν_t = kinematic eddy viscosity ($m^2\ s^{-2}$)

ρ = water density ($kg\ m^{-3}$)

σ_k, σ_ω = k-ω SST closure coefficient

$\overline{\tau}_{ij}$ = fluid stress tensor ($N\ m^{-2}$)

τ_w = wall shear stress ($N\ m^{-2}$)

ω = screw rotation speed ($rad\ s^{-1}$)

ω_t = specific dissipation rate (s^{-1})

References

[1] K.-A. Radlik, *Hydrodynamic screw for energy conversion - uses changes in water supply to regulate energy output*, 1997, .

[2] S.R. Waters, *Analysing the performance of the Archimedes Screw Turbine within tidal range technologies*, Lancaster University, 2015.

[3] J. Adlard, *Archimedes' screw: Copley Hydropower Generator*, Future Energy Yorkshire, Yorkshire, 2011.

[4] *Archimedean Screw Turbine*. Spaans Babcock Hydro Power, Balk, 2012.

[5] O.M. Dada, I.A. Daniyan and O.. Adaranola, *Optimal Design of Micro Hydro Turbine (Archimedes Screw Turbine) in Arinta Waterfall in Ekiti State, Nigeria*, 4 (2014), pp. 34–38.

[6] *Maintaining Archimedes Screw Pumps*. Available at http://www.ecsengineeringservices.com/maintaining-archimedes-screw-pumps/.

[7] *Archimedes Screw Pumps*. ECS Engineering Services, Sutton-in-Ashfield, 2016.

[8] C.D. McNabb, C.R. Liston and S.M. Borthwick, *Passage of Juvenile Chinook Salmon and other Fish Species through Archimedes Lifts and a Hidrostal Pump at Red Bluff, California*, Trans. Am. Fish. Soc. 132 (2003), pp. 326–334.

[9] T.B. Havn, S.A. Sæther, E.B. Thorstad, M.A.K. Teichert, L. Heermann, O.H. Diserud et al., *Downstream migration of Atlantic salmon smolts past a low head hydropower station equippped with Archimedes screw and Francis turbines*, Ecol. Eng. 105 (2017), pp. 262–275.

[10] P. Kibel, *Archimedes Screw Turbine Fisheries Assessment. Phase II: Eels and Kelts*, Moretonhampstead, Devon, 2008.

[11] United Kingdom Environment Agency, *Hydropower Good Practice Guidelines Screening requirements*, York, England, 2012.

[12] C.A. Boys, B.D. Pfugrath, M. Mueller, J. Pander, Z.D. Deng and J. Geist, *Physical and hydraulic forces experienced by fish passing through three different low-head hydropower turbines*, Mar. Freshw. Res. (2018), pp. 1934–1944.

[13] M. Denny, *The efficiency of overshot and undershot waterwheels*, Eur. J. Phys. 25 (2004), pp. 193–202.

[14] A. Lashofer, W. Hawle and B. Pelikan, *State of technology and design guidelines for the Archimedes screw turbine*, Univ. Nat. Resour. Life Sci. Vienna (2012), pp. 1–8.

[15] C. Rorres, *The Turn of the Screw: Optimal Design of and Archimedes Screw*, J. Hydraul. Eng. 126 (2000), pp. 72–80.

[16] S. Simmons, K. Songin and W. Lubitz, Experimental investigation of the factors affecting Archimedes screw generator power output, in HYDRO 2017 (7-11 October 2017), 2017.

[17] K. Songin, *Experimental Analysis of Archimedes Screw Turbines*, University of Guelph, 2017.

[18] D. Nuernbergk, *Wasserkraftschnecken - Berechnung Und Optimaler Entwurf von Archimedischen Schnecken Als Wasserkraftmaschine (Hydropower Screws - Calculation and Design of Archimedes Screws Used in Hydropower)*, 1st ed.Verlag Moritz Schäfer, Detmold, 2012.

[19] W.D. Lubitz, M. Lyons and S. Simmons, *Performance Model of Archimedes Screw Hydro Turbines with Variable Fill Level*, J. Hydraul. Eng. 140 (2014), pp. 1–11.

[20] D.M. Nuernbergk and C. Rorres, *An Analytical Model for the Water Inflow of an Archimedes Screw Used in Hydropower Generation*, J. Hydraul. Eng. 139 (2012), pp. 120723125453009.

[21] K.J. Songin and W.D. Lubitz, *Measurement of fill level and effects of overflow in power-generating Archimedes screws*, J. Hydraul. Res. 57 (2018), pp. 635–646.

[22] M. Lisicki, W. Lubitz and G.W. Taylor, *Optimal design and operation of Archimedes screw turbines using Bayesian optimization*, Appl. Energy 183 (2016), pp. 1404–1417.

[23] A. Kozyn and W. Lubitz, *Experimental Validation of Gap Leakage Flow Models in Archimedes Screw Generators*, in *Renewable Energy in the Service of Mankind Vol I*, Sayigh A., ed., Springer International Publishing Switzerland, Cham, 2015, pp. 365–375.

[24] M. Lyons and W.D. Lubitz, Archimedes screws for microhydro power generation, in Proceedings of the ASME 2013 7th International Conference on Energy Sustainability

& 11th Fuel Cell Science, 2013, pp. 1–7.

[25] J. Rohmer, D. Knittel, G. Sturtzer, D. Flieller and J. Renaud, *Modeling and experimental results of an Archimedes screw turbine*, Renew. Energy 94 (2016), pp. 136–146.

[26] G. Dellinger, A. Terfous, P.-A. Garambois and A. Ghenaim, *Experimental investigation and performance analysis of Archimedes screw generator*, J. Hydraul. Res. 1686 (2016), .

[27] S. Simmons, *A Computational Fluid Dynamic Analysis of Archimedes Screw Generators*, University of Guelph, 2018.

[28] A. Kozyn, *Power Loss Model for Archimedes Screw Turbines*, University of Guelph, 2016.

[29] C.W. Hirt and B.D. Nichols, *Volume of Fluid (VOF) Method for the Dynamics of Free Boundaries*, J. Comput. Phys. 39 (1981), pp. 201–225.

[30] F.R. Menter, *Two-equation eddy-viscosity turbulence models for engineering applications*, AIAA J. 32 (1994), pp. 1598–1605.

[31] S.M. Damian, *Description and utilization of interFoam multiphase solver*, 2004.

[32] B. van Leer, *Towards the ultimate conservative difference scheme. II. Monotonicity and conservation combined in a second-order scheme*, J. Comput. Phys. 14 (1974), pp. 361–370.

[33] T.P. Dhakal and D.K. Walters, Curvature and Rotation Sensitive Variants of the K-Omega SST Turbulence Model, in ASME 2009 Fluids Engineering Division Summer Meeting, 2010, pp. 2221–2229.

[34] J. Bardina, P. Huang and T. Coakley, *Turbulence modeling validation, testing, and development*, NASA Tech. Mem./Moffet Field, USA, 1997.

[35] F. Liu, A Thorough Description of How Wall Functions are Implemented in OpenFOAM, in Proceedings of CFD with OpenSource Software, 2016.

[36] F. Russo and N.T. Basse, *Scaling of turbulence intensity for low-speed flow in smooth pipes*, Flow Meas. Instrum. 52 (2016), pp. 101–114.

[37] K.G. Mooney, T. Maric and J. Höpken, *The OpenFOAM Technology Primer*, SourceFlux, Duisburg, Germany, 2014.

[38] H. Yang, *Advanced turbulence models for recirculating flows*, Texas Tech University, 1994.

[39] A. Kamath, G. Fleit and H. Bihs, *Investigation of Free Surface Turbulence Damping in RANS Simulations for Complex Free Surface Flows*, Water 11 (2019), pp. 1–26.